

Neural PDE Solvers for Irregular Domains

Biswajit Khara^{1†}, Ethan Herron^{1†}, Zhanhong Jiang⁴, Aditya Balu², Chih-Hsuan Yang¹,
Kumar Saurabh¹, Anushrut Jignasu¹, Soumik Sarkar^{1,2}, Chinmay Hegde³,
Adarsh Krishnamurthy^{1,2}, Baskar Ganapathysubramanian^{1,2*}

¹ Department of Mechanical Engineering, Iowa State University, Iowa, USA 50011

² Translational AI Center, Iowa State University, Iowa, USA 50011

³ Computer Science Department, New York University, New York, USA 10012

⁴ Johnson Control Inc.

* Corresponding author: baskarg@iastate.edu

† Authors contributed equally

Abstract

Neural network-based approaches for solving partial differential equations (PDEs) have recently received special attention. However, the large majority of neural PDE solvers only apply to rectilinear domains, and do not systematically address the imposition of Dirichlet/Neumann boundary conditions over irregular domain boundaries. In this paper, we present a framework to neurally solve partial differential equations over domains with irregularly shaped (non-rectilinear) geometric boundaries. Our network takes in the shape of the domain as an input (represented using an unstructured point cloud, or any other parametric representation such as Non-Uniform Rational B-Splines) and is able to generalize to novel (unseen) irregular domains; the key technical ingredient to realizing this model is a novel approach for identifying the interior and exterior of the computational grid in a differentiable manner. We also perform a careful error analysis which reveals theoretical insights into several sources of error incurred in the model-building process. Finally, we showcase a wide variety of applications, along with favorable comparisons with ground truth solutions.

1 Introduction

Motivation Most physical phenomena are modeled using a set of governing partial differential equations (PDEs). Numerical methods—finite difference (FDM), finite element (FEM), and spectral methods—for solving PDEs discretize the physical domain (into cells, elements, etc.) and *approximate* the solution over this discretized domain using select families of basis functions [1–3]. A significant part of PDE solver technology involves solving PDEs on complex, irregular domains (for instance, flow across aerofoils in aeronautics or patient-specific organ geometries in medical diagnostics). This is a major challenge, as articulated in the NASA CFD 2030 [4] vision (“Mesh generation and adaptivity continue to be significant bottlenecks...”). In particular, capturing the complex geometry, as well as rigorously accounting for the non-trivial boundary conditions on these complex geometries, has driven careers in mesh generation and PDE solver technology.

Motivated by these challenges, this paper addresses the following problem, “Can we design a neural PDE solver that can produce field solutions across arbitrary geometries?”. We do so by utilizing an analytical approach developed in the computational mechanics community—the immersed boundary method (IBM) [5, 6]. In such approaches, the irregular geometry is ‘immersed’ in a regular grid, thus allowing standard meshes to model irregular geometries. We extend this powerful approach to neural PDE solvers, which enables the creation of PDE solvers that can produce field solutions for a distribution of irregular geometries. We show that such an approach also allows the natural incorporation of different boundary conditions over complex geometries; as a side benefit, our approach also allows us to compute *a priori* error estimates using a combination of techniques from neural net generalization and finite element analysis.

Neural PDE Solvers Since neural networks are powerful nonlinear function approximators, there has been a growing interest in using neural networks to solve PDEs [7–20]. Unlike numerical methods, many of these methods do not require a mesh. But a common challenge most neural PDE solvers face is the efficient imposition of boundary conditions, especially on non-cartesian boundaries [21]. Furthermore, among collocation-based neural solvers, the satisfaction of certain regularity conditions becomes non-trivial to impose [22].

Immersed Approach Classical numerical methods such as finite difference (FDM) or finite element methods (FEM) generally employ a grid or mesh to discretize the domain geometry and function space. Solving PDEs defined on complex geometries requires a mesh to be prepared before the analysis. This step, commonly known as the “mesh generation” step, is non-trivial and often expensive. Immersed methods [5, 23] are one way to overcome this challenge. The computational grid is simplified in immersed methods by considering a rectilinear axis-aligned grid that encloses the irregular geometry (within which we seek a PDE solution). The irregularly-shaped geometry is then “immersed” in this background mesh (see Fig. 1). Thus, a part of the background mesh forms the actual computational mesh; the rest of the background mesh is considered exterior, and thus not used in the computation of the PDE solution.

In this work, we combine the generalization capability of deep neural networks to solve PDEs defined on irregularly-shaped domains using ideas from immersed finite element methods [23–25]. In recent years, immersed methods have been favored for massive parallel implementations since all computations are performed on a regular grid [6, 26–28]. This fact translates to tensor-based operations in convolutional neural networks, which otherwise are unsuitable for dealing with complex geometrical contours. A key ingredient is the careful design of the loss function, along with a mechanism to determine the interior/exterior (in-out) of the computational domain. Our main contributions are as follows:

1. **[Framework]:** We present a parametric PDE-based loss function that learns robust and watertight boundary conditions imposed by complex geometries. Using this loss function, we train a deep neural network—Immersed Boundary Network (IBN)—that uses the geometric information as input to predict a field solution that satisfies the governing PDE over the arbitrary domain. We show that a single trained IBN can produce solutions to a PDE across a distribution of arbitrary shapes.
2. **[Error Analysis]:** We provide analysis of convergence and generalization error bounds of the proposed PDE-based loss function with the immersed approach.
3. **[Applications and Broader Impact]:** Finally, we use this parametric PDE-based loss function to learn solutions of PDEs over irregular geometries. We illustrate the approach on two PDEs—Poisson and Navier-Stokes—and a host of irregular geometries in 2D and 3D. IBN opens up fast design exploration and topology optimization for various societally critical applications such as shape design for energy harvesters, and aerodynamic design of vehicles.

2 Mathematical Preliminaries

Consider domain $\Omega_B \subset \mathbb{R}^d$ ($d \in \{2, 3\}$) with a rectilinear boundary Γ_B ; and another domain $\Omega_o \subset \Omega_B$ with an irregular boundary Γ_o . Without loss of generality, the d -dimensional unit interval $[0, 1]^d$ can be considered an example of Ω_B . Define $\Omega = \Omega_B / \Omega_o$ (see Figure 1a for an illustration in 2D Euclidean space). On this non-rectilinear domain Ω , we now consider an abstract PDE (Eq 1a)

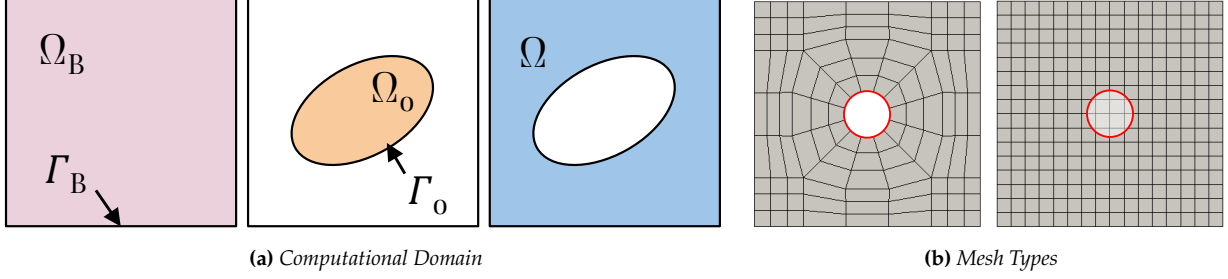


Figure 1: (a) Schematic of a typical domain for the background mesh Ω_B (with boundary Γ_B), the embedded/immersed object Ω_o (with boundary Γ_o) and the computational domain Ω . (b) A “body-fitted” mesh that discretely conforms to the object and an object embedded/immersed in a background mesh. This paper focuses on immersed type meshes with different object geometries.

with general boundary conditions (Eq 1b) given by:

$$\mathcal{N}(u) = f(\underline{x}) \text{ in } \Omega, \quad (1a)$$

$$\mathcal{A}(u) + \mathcal{D}(\nabla u) = g \text{ on } \Gamma_o \subset \partial\Omega. \quad (1b)$$

Here, u is an unknown function such that $u : \Omega \mapsto \mathbb{R}$, \mathcal{N} is a differential operator (possibly nonlinear) and $f(\underline{x})$ is a known function of the domain variable $\underline{x} \in \Omega$. The boundary conditions are defined by operators \mathcal{A} and \mathcal{D} . In this paper, we look at two concrete examples of Equation 1: Poisson and Navier-Stokes equations.

Poisson Equation: Poisson equation is frequently used to model steady-state mass/heat diffusion, electrostatics, surface reconstruction, etc. and is given by:

$$-\Delta u = f \text{ in } \Omega, \quad (2a)$$

$$\alpha u + \beta \nabla u \cdot \underline{n} = g \text{ on } \Gamma, \quad (2b)$$

where $u : \Omega \rightarrow \mathbb{R}$ is a scalar function that, depending on the underlying physics, represents the mass density, temperature, electric potential, or the surface indicator function, respectively. A spectrum of boundary conditions (Dirichlet, Neumann, Robin) are produced by varying the scalars α and β .

Navier-Stokes Equations: The Navier-Stokes equations are widely used to model fluid flow. The steady incompressible Navier-Stokes equations are given by:

$$\underline{u} \cdot \nabla \underline{u} - \nu \Delta \underline{u} + \nabla p = \underline{f} \text{ in } \Omega \quad (3a)$$

$$\underline{u} = \underline{g} \text{ on } \Gamma \quad (3b)$$

where $\underline{u} : \Omega \rightarrow \mathbb{R}^d$ is a vector valued function that represents the velocity field, and $p : \Omega \rightarrow \mathbb{R}$ is a scalar representing the pressure in the fluid. The coefficient ν is the viscosity of the fluid.

Immersed Finite Element Method: In this paper, we formulate our neural PDE solver based on an immersed FEM discretization. In terms of the notations developed above, we discretize Ω_B using an axis-aligned grid (Figure 1b (right)) and we call this a “background mesh”. To incorporate the effect of Ω_o , the boundary curve Γ_o is considered “immersed” in this background mesh, and the boundary conditions on Γ_o are applied approximately (in a weak manner) on the grid points that fall near this curve. The details of how the boundary conditions are applied are discussed in Section 3.

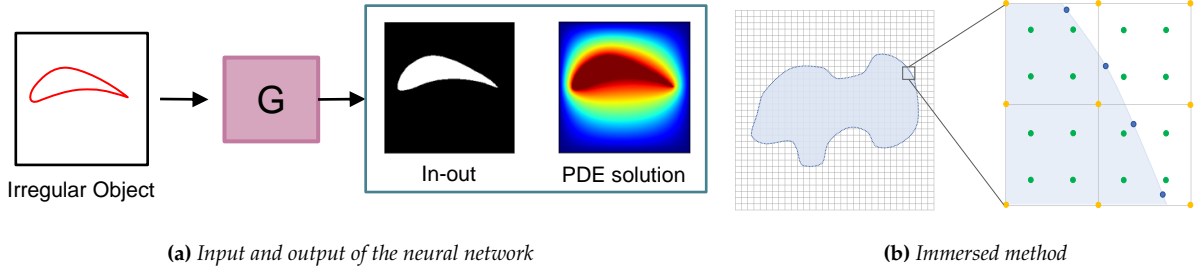


Figure 2: (a) The input to the network G is a representation of the object, possibly a point cloud or a NURBS curve/surface. A trained network can then predict the in-out information of the object and the field solution. (b) A visual representation of the irregular object intersecting the element. Each yellow dot denotes the pixels; green dots denote the Gauss points used to interpolate the value of the finite element; blue dots denote points from the object boundary. The shaded region is the area inside the boundary.

3 Our Approach: Immersed Boundary Network (IBN)

We will learn an immersed boundary network (IBN) that produces a (field) solution to a given PDE and also (rigorously) adheres to the boundary conditions imposed by a family of complex geometries.

Our IBN model is written as a parameterized function $G(\{P\};\theta)$, where θ is a set of tunable network weights, and $\{P\}(\subset \Gamma_o)$ represents the geometry (it can either be in the form of a point cloud or a set of NURBS control points representing the boundary of the complex geometry Γ_o). Given such an input $\{P\}$, a trained network G should be able to predict both the interior/exterior of the computational domain and the solution to the PDE. Thus, the neural mapping is more precisely defined as $G(\{P\};\theta) : \mathbb{R}^{n \times d} \times \mathbb{R}^{|\theta|} \rightarrow \mathbb{R}^{N \times (1+n_{dof})}$, where n is the cardinality of $\{P\}$, d is the spatial dimension, N is the number of points used to discretize the mesh and n_{dof} is the number of unknowns in the PDE (e.g., $n_{dof} = 1$ for Poisson's equation, and $n_{dof} = (d + 1)$ for Navier-Stokes equations). Suppose \mathbf{U} is the discrete approximation of the solution field u and χ a discrete representation of the occupancy function that indicates which points on the background mesh are interior/exterior to the immersed object. Then, given $\{P\}$, we have $[\chi, \mathbf{U}] = G(\{P\};\theta)$, where $\chi \in \mathbb{R}^{N \times 1}$ and $\mathbf{U} \in \mathbb{R}^{N \times n_{dof}}$, and the network architecture used to encode the geometry information can be either an MLP (for NURBS curves/surfaces) or Graph Convolution layers (for point clouds etc.). Further, for predicting fields, we use 2D/3D transpose convolution and upsampling layers (more details provided in Supplement).

3.1 Numerical Framework

We rely on a FEM discretization (\mathbf{U} , defined above) of the field solution as well as its spatial derivatives. Let \mathcal{K}^h be a discretization of Ω_B into n_{el} finite elements K_i such that $\cup_{n_{el}} K_i = \Omega_B$ (Note, n_{el} finite elements produce N nodes, each of which have n_{dof} predicted field values, resulting in the cardinality of the prediction of G). Following standard FEM analysis, we define a function space $V^h = \{v^h \in V : v^h|_K \in Poly_m(K), K \in \mathcal{K}^h\}$, where $Poly_m(K)$ denotes the set of polynomial functions of degree m defined on K . Since we are dealing with an immersed finite element method, \mathcal{K}^h is composed of a rectilinear axis-aligned grid with N nodes. Now, suppose $\{\mathcal{B}_i(\underline{x})\}_{i=1}^N$ is a suitable basis that span V^h . Any function $u^h \in V^h$ can be written as

$$u^h(\underline{x}) = \sum_{i=1}^N \mathcal{B}_i(\underline{x}) U_i, \quad (4)$$

where U_i are the solution values at the nodal points in the mesh \mathcal{K}^h , with $\mathbf{U} = \{U_1, \dots, U_i, \dots, U_N\}$. In the sequel, when we refer to the discrete approximation of the solution, we mean either u^h (the

functional representation) or the discrete set of nodal values $\{U_i\}$ (the vector representation). The two will be used interchangeably, assuming that the underlying basis functions $\mathcal{B}(\underline{x})$ are known.

3.2 Training Loss Function

A key novelty of our method lies in formulating an appropriate PDE loss function for irregular geometries and their associated numerics. At a high level, our loss consists of two parts: one addressing the given PDE and the other addressing the boundary conditions imposed by (complex, irregular) geometries. Thus we can break down the overall loss function into two main components: (i) predicting the field u^h (PDE Loss), and (ii) predicting the occupancy function χ and exact imposition of boundary conditions (Geometry Loss).

3.2.1 PDE Loss

The PDE component of the loss function is standard and follows directly from the Galerkin formulation of the given PDE. For the abstract PDE in Equation 1, the corresponding Galerkin formulation (with boundary conditions weakly satisfied) is to find $u^h \in V^h$ such that

$$\left(v^h, [\mathcal{N}(u^h) - f]\right)_{\Omega} + \lambda \left(v^h, [\alpha u^h + \beta \nabla u^h \cdot n - g^h]\right)_{\Gamma} = 0, \quad \forall v^h \in V^h. \quad (5)$$

In general, if a unique u^h exists, then for any other function $w^h \in V^h$ ($w^h \neq u^h$) will make the right hand side of Equation 5 nonzero. We call this the residual of Equation 5, i.e.,

$$R = \left(v^h, [\mathcal{N}(w^h) - f]\right)_{\Omega} + \lambda \left(v^h, [\alpha w^h + \beta \nabla w^h \cdot n - g^h]\right)_{\Gamma}, \quad (6)$$

where, $w^h \in V^h$. Minimizing this residual should provide us with a unique solution. Unfortunately, we cannot perform integrations over Ω in a straightforward manner, but we can do so on Ω_B . On the other hand, Ω_B also contains Ω_o but we do not want to perform integrations on Ω_o . We resolve this via the occupancy function χ^h , which helps us perform integrations on Ω_B while at the same time enforcing no contribution from Ω_o to R .

3.2.2 Geometry Loss

This corresponds to imposition of boundary conditions on the surface defined by points $\underline{p}_i \in \{P\} \subset \Gamma_o$ and correct prediction of the occupancy function χ . For given surface points \underline{p}_i , the discrete solution $u^h(\underline{x})$ on these boundary points is $u(\underline{p}_i) = \sum_{j=1}^N \mathcal{B}_j(\underline{p}_i) U_j \quad \forall \underline{p}_i \in \{P\}$. This interpolation (separate from the Gauss points, see Figure 2(b)) helps us exactly impose the boundary conditions. (More details on the interpolation are explained in Supplement).

Predicting the occupancy function χ can be obtained using two approaches: (i) computing winding numbers, or (ii) solving the Eikonal equation as another unknown.

Generalized Winding Number: This is the general form of the winding number which counts the number of loops of the boundary around any point \underline{x} . The generalized winding number can be calculated as the surface integral of the differential solid angle ($\int_{\Gamma_o} dS(\underline{x})$) [29]. Given a boundary representation of an object, we can use the generalized winding number to determine in-out information since any point inside the object boundary will have a winding number 1. The in-out occupancy χ_w is calculated as:

$$\chi_w(\underline{x}) = \sum_{i=1}^n a_i \frac{(\underline{p}_i - \underline{x}) \cdot \hat{n}_i}{4\pi \|\underline{p}_i - \underline{x}\|^3} \quad (7)$$

where a_i is the Voronoi area of a given point and \hat{n}_i is the normal for a given point \underline{p}_i [29]. Using χ_w , we can obtain all nodes inside the geometry ($u^h \in \Omega_o$) by using χ_w as a masking function. Since

this is deterministically obtained, the network G only predicts $N \times n_{dof}$ values. However, there are some limitations of χ_w not being robust to noise. Hence, an alternate approach using signed distance fields (SDF) has recently become popular.

Eikonal Equation: SDF (ϕ) denotes the distance to the closest point on the surface Γ_o . The sign of the distance fields can be used as occupancy information ($\chi_e = \text{sign}(\phi)$). The signed distance field is obtained by solving the viscosity stabilized version of the Eikonal equation ($(1 + \tau)\|\nabla\phi\| - \tau(\nabla\phi) = 1$, $\tau \in [0, 0.5]$) [30]. For this, the network G , will predict one additional field, i.e., $N \times (1 + n_{dof})$ values, unlike the Winding number-based approach. In this work, we demonstrate the usage of both χ_e and χ_w for obtaining the mask and applying the boundary conditions.

Combining the PDE Loss and the Geometric Loss, the complete loss function is:

$$\mathcal{J}(w^h) = \underbrace{\|R(w^h)\|_2}_{\text{PDE loss}} + \lambda_1 \underbrace{\sum_{i=1}^n |\alpha w^h(\underline{x}_i) + \beta \nabla w^h(\underline{x}_i) \cdot n - g_i|^2}_{\text{boundary condition on object}} + \lambda_2 \underbrace{\sum_{j \in \{j|\chi > 0\}} |w^h - g_{in}|^2}_{\text{exterior points}}, \quad (8)$$

where g_i and g_{in} represent suitable functions defined in Γ_o and Ω_o respectively. We assume that g_i conforms to the boundary Γ_o . i.e., the point cloud is not noisy, and the boundary conditions are applied accurately. Thus we can then define the minimization problem statement as

$$u^h = \arg \min_{w^h \in V^h} \mathcal{J}(w^h). \quad (9)$$

which can be approximately solved using multiple gradient descent steps. To summarize, the first term in Equation 8 represents the loss function derived from the PDE, the second term attempts to “weakly” set the boundary points to their respective prescribed values, and finally, the third term attempts to set the object interior points to a fixed value conforming to the object boundary. Appropriate values for λ_1 and λ_2 are generally problem dependent, but for our experiments we take $\lambda_1 = \lambda_2 = O(1)$. However, in case of high gradient in the solution values near boundaries, these coefficients scale $\propto \frac{1}{h}$. This closely aligns with the results for these coefficients from the analysis of the IBM [31, 32].

4 Error Analysis

In this section, we summarize theoretical results for the convergence behavior and the generalization error for IBN. Due to tight space constraints, all detailed proofs are relegated to the supplementary material. A summary of the theoretical results is presented in Table 1.

For a given geometry Γ_o , we denote u as the original optimum solution to the PDE and u^h be the optimal solution at discretization level h ; these are functions evaluated at any point $\underline{x} \in \Omega$. From classical FEM analysis, we will bound the discretization error $\|u^h - u\|$ as a function of h . Now, the field predicted by the network $G(\{P\}, \theta)$ is typically an inaccurate version of u_h , and we can express the error e_G as follows:

$$\|e_G^k\| = \|u_{\theta_k} - u\| = \|u_{\theta_k} - u_{\theta^*} + u_{\theta^*} - u^h + u^h - u\| \quad (10)$$

where, u_{θ_k} is the field solutions corresponding to the network parameters θ_k at the k^{th} iteration of the optimization and u_{θ^*} is the theoretical optimum (i.e., a limit point) of u_{θ_k} .

We analyze the quadratic form of $\|e_G^k\|$, i.e., $\|e_G^k\|^2$; in the stochastic setting, the relevant quantity is the second moment, i.e., $\mathbb{E}[\|e_G^k\|^2]$. By applying the fundamental inequality $\|a + b + c\|^2 \leq$

Table 1: Summary of different generalization bounds. Please refer to the Appendix for the detailed derivation of Corollary 13 and Corollary 16.

| Statement | Setting | Property | Step Size | Rate |
|--------------|------------|-------------------------|-------------|---|
| Corollary 5 | Batch | μ -strong convexity | Constant | $\mathcal{O}\left(N^2\rho_1^K + \frac{1}{(NK)^\alpha}\right)$ |
| Corollary 13 | Stochastic | μ -PL condition | Constant | $\mathcal{O}\left(N^2\rho_2^K + N^2\sigma^2 + \frac{1}{(NK)^\alpha}\right)$ |
| Corollary 16 | Stochastic | μ -PL condition | Diminishing | $\mathcal{O}\left(\frac{N^2}{K} + \frac{1}{(NK)^\alpha}\right)$ |

¹ μ : the strongly convex constant defined in the later section;

² N : the number of basis functions; ³ $\rho_1, \rho_2 \in (0, 1)$; ⁴ K : the number of epochs; ⁵ α : the polynomial order of FEM basis functions; ⁶ PL: Polyak-Lojasiewicz; ⁷ σ : second moment constant.

$3(\|a\|^2 + \|b\|^2 + \|c\|^2)$, we can obtain

$$\|e_G^k\|^2 \leq 3\left(\underbrace{\|u_{\theta_k} - u_{\theta^*}\|^2}_{\text{Optimization error}} + \underbrace{\|u_{\theta^*} - u^h\|^2}_{\text{Modeling error}} + \underbrace{\|u^h - u\|^2}_{\text{Discretization error}} \right). \quad (11)$$

Thus the generalization error is bounded above by three different terms, which are respectively the *optimization error*, *modeling error*, and *discretization error*. The discretization error is only dependent on the choice of the discretization and the modeling error is based on the choice of the network architecture and hence both the errors remains static through out the optimization.

To facilitate the understanding of how $\|e_G^k\|^2$ converges and to simplify the analysis, we will next combine the optimization error and modeling error, while following standard FEM analysis to bound the discretization error. We make the following assumptions.

Assumption 1. There exists a constant $c > 0$ such that $\|u_{\theta^*} - u^h\| \leq c\|u_{\theta_k} - u_{\theta^*}\|, \forall k \geq 0$.

Assumption 1 implies that the modeling error can be upper bounded by the optimization error up to a constant. This should be possible since we can always find some constant c to ensure that the above assumption holds. Therefore, we now obtain

$$\|e_G^k\|^2 \leq 3[(1 + c^2)\|u_{\theta_k} - u_{\theta^*}\|^2 + \|u^h - u\|^2]. \quad (12)$$

Assumption 2. There exists a constant $L > 0$ such that for all $\underline{x}, \underline{y} \in \mathbb{R}^d$, $\|U_i(\underline{x}) - U_i(\underline{y})\| \leq L\|\underline{x} - \underline{y}\|$, for all $i \in \{1, 2, \dots, N\}$.

Assumption 2 implies that the prediction function provided by IBN is Lipschitz continuous [33], which signifies the robustness of the predictions obtained from deep neural networks under perturbations of the network parameters. This is a standard assumption made during the analysis of neural network generalization.

We first investigate the convergence rate when \mathcal{J} is *strongly convex and in a batch setting*. Notice that all terms in Equation 8, including the boundary loss (which is L_2 loss of the imposed boundary conditions) and the PDE residual loss (from variational arguments) are strongly convex.

Lemma 3. Assume that the basis function $\mathcal{B}_i(\underline{x})$ are chosen such that they are at least continuously differentiable locally over a mesh. Then the following relationship holds true:

$$\|u^h - u\|^2 \leq Ch^{2\alpha}, \quad (13)$$

where $C > 0$ and α is the order of continuous derivative. Typically, $\alpha \geq 1$.

Theorem 4. Suppose that \mathcal{J} is μ -strongly convex and β -smooth. Let Assumptions 1 and 2 hold. By applying the gradient descent algorithm with a constant step size $\eta_k = \eta = \frac{2}{\mu + \beta}$, the generalization error $\|e_G^K\|^2$ satisfies the following relationship after K epochs,

$$\|e_G^K\|^2 \leq 3(1 + c^2)L^2N^2\hat{\mathcal{B}}^2 \left(1 - \frac{2}{\kappa + 1}\right)^{2K} \|\theta_0 - \theta^*\|^2 + 3Ch^{2\alpha}, \quad (14)$$

where c, N are defined in Assumptions 1 and 2, μ is the strong convexity constant, β is the smoothness constant, L is the Lipschitz continuous constant, $\hat{\mathcal{B}}$ is the upper bound of the basis function $\mathcal{B}_i(\underline{x})$, $\kappa = \frac{\beta}{\mu}$ is the condition number, and θ_0 and θ^* are respectively the initialization and optimum of θ .

Theorem 4 implies that the generalization error of IBN is upper bounded by two terms, with the first term related to the optimization error and the second term the static error due to the discretization. Additionally, in an asymptotic manner, we have that

$$\lim_{K \rightarrow \infty} \|e_G^K\|^2 \leq 3Ch^{2\alpha}, \quad (15)$$

which suggests that the generalization error will ultimately be dominated by the discretization error determined by the resolution h and the order of the FEM basis function α (here $\alpha = 1$), both of which rely on the definition of basis functions $\{\mathcal{B}_i(\underline{x})\}_{i=1}^N$. If h is chosen such that $h = \mathcal{O}(\frac{1}{\sqrt{KN}})$ (justified by [34]), the following corollary can be obtained:

Corollary 5. Suppose that $h = \mathcal{O}(\frac{1}{\sqrt{KN}})$. Given all conditions and parameters from Theorem 4, the generalization error achieves an overall sublinear convergence rate

$$\|e_G^K\|^2 \leq \mathcal{O}\left(N^2\rho_1^K + \frac{1}{(NK)^\alpha}\right). \quad (16)$$

where ρ_1 is a constant smaller than 1.

In summary, our upper bound on the generalization error can be separated into two terms, both of which converge to zero as the number of training epochs K become large — provided the discretization is also chosen inversely with K . Qualitatively, the above bound provides a thumb rule to set the discretization of the mesh, h , based on available computation time (measured in the number of epochs K) and the desired error level e_G . From a practical perspective, the bound allows estimation of resource requirement for a desired discretization and error level.

5 Experimental Results

In this section, we provide results from our proposed immersed neural approach. We highlight single instance field solutions for Poisson’s and Navier-Stokes equations and the field solutions to Poisson’s equation for a family of randomly generated shapes. As previously mentioned, the IBN framework can map geometry representation to the field solution of a given PDE. While the geometry representation could be an unstructured point cloud or other structured representations such as NURBS control points, the PDE field solution is represented as a uniform grid. We use a single Nvidia Tesla P40 GPU in all the experiments shown below. Each network used the Adam optimizer with a learning rate of 3e-4. Further, as explained in Section 3.2.2, we have two approaches for obtaining the occupancy information(χ). A comparison between both the methods is provided in the Supplement, and we only show generalized winding number-based results here.

Solution to Poisson’s Equation in 2D and 3D:

For solving Poisson’s Equation in 2D, we first generate a large geometry data (a family of NURBS curves sampled randomly). We ensure that the shapes are smooth and do not have any discontinuities and self-intersections. Once the shapes are generated, we obtain point clouds composed of 1,000 points, and all field solutions were represented using a 128×128 resolution grid (represented as an image). Our neural network to map the point cloud to the image domain was composed of 6 MLP layers followed by 8 layers of convolution and transpose convolution operations. Here, we choose simple MLP layers, but more sophisticated architectures such as DGCNNs could also be used. Figure 3(a) shows the results for one of the test geometries (the occupancy information χ and the solution to Poisson’s equation U).

The same problem can be solved using 3D parametric datasets such as the ABC dataset, ShapeNet, etc. We use a subset of geometries from the ABC dataset to show results here. The process remains the same, except for the resolution of the grid being $196 \times 196 \times 196$ in 3D. Figure 3(b) shows one of the 3D geometries used (an Engine), the corresponding domain, and the volume rendering of the neural solution to the Poisson’s equation.

Convergence Analysis:

To check the accuracy of our method, we solve Poisson’s equation Equation 2 on a circular disk of radius $R = 0.25$ immersed in a unit square. The forcing function $f = 1$ on the disk, and the boundary condition is specified as $u = 0$ at the perimeter of the disk. Therefore, $\Omega_o = \{r < R\}$ and $\Gamma_o = \{r = R\}$. The exact solution to this problem is given by $u(r) = \frac{1}{4}(R^2 - r^2)$, where $r = \sqrt{x^2 + y^2}$ is the radial position of a point on the disk.

We discretize the unit square domain using an $N \times N$ grid, and the object boundary Γ_o is represented using a point cloud. We optimize the loss function mentioned in Section 3 to obtain the solution. The results are presented in Figure 4. Figure 4a shows the contours of the discrete solution u^h , the exact solution u and the error $e = u^h - u$, for $N = 128$. Figure 4b shows the L^2 -norm of the error with mesh size h in a log-log plot. We see first-order convergence with increasing resolution, which matches established theory from IBM analysis ([31] (Lemma 37.2) and [32]).

Navier-Stokes Equation:

We also validate our framework against a canonical flow past an airfoil using the steady Navier-Stokes equations (NSE) introduced in Equation 3. The flow field output from IBN shows the

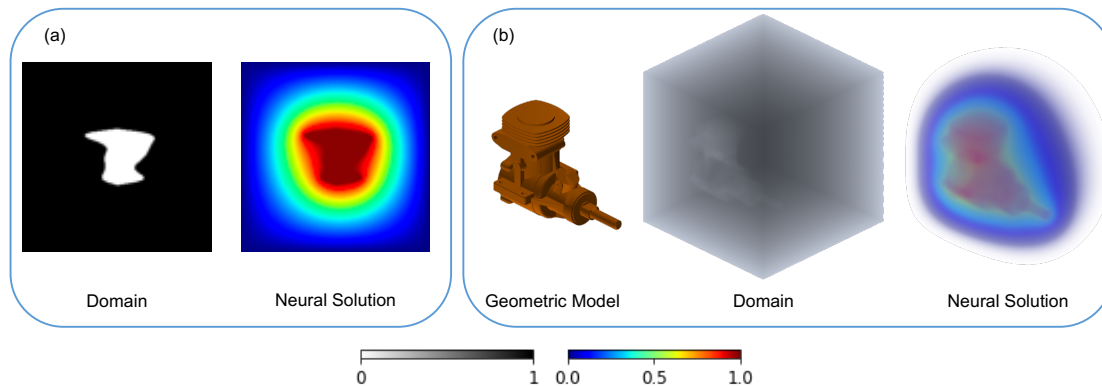


Figure 3: (a) Left: The in-out of the domain for the immersed solve. Right: Solution to the Poisson’s equation with an immersed object in 2D. (b) Left: The geometry model being immersed. Center: The in-out information. Right: Solution to Poisson’s equation using the IBN framework.

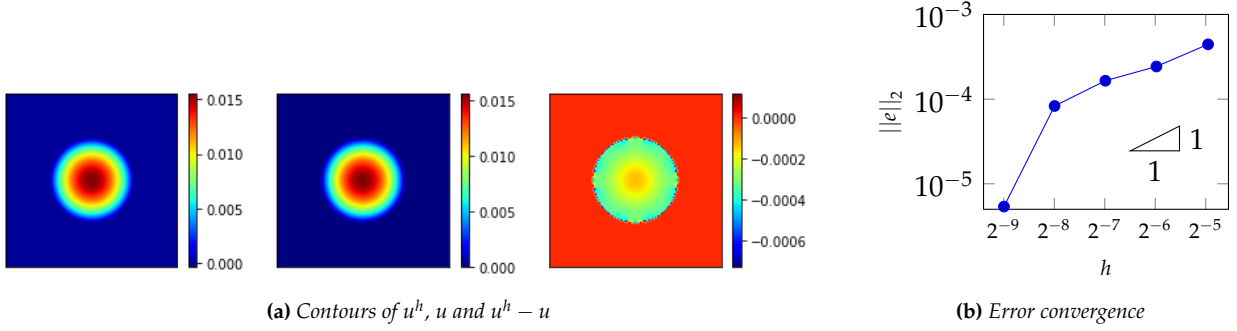


Figure 4: Error convergence with linear basis ($\alpha = 1$) for the Poisson's equation solved on a circular disk of radius $R = 0.25$.

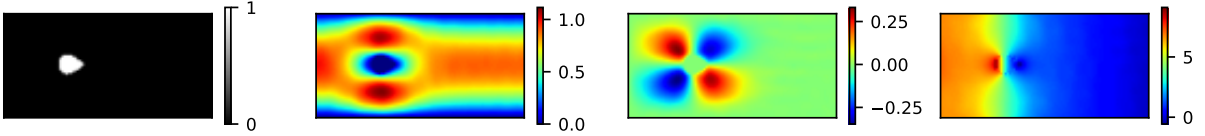


Figure 5: Immersed method with object mask applied to solve the Navier-Stokes equation for a steady flow past a NACA 0012 aerofoil. (left) domain/boundary mask (middle left) x velocity, (middle right) y velocity, and (right) pressure.

expected wake structure (at Reynolds number 40), is symmetric about the mid-plane, shows the stagnant pressure point on the upwind side of the immersed object, and satisfies the imposed no-slip condition.

The boundary conditions for this problem are:

$$x = 0 : u_x = 1 - \left(\frac{2y}{H} - 1\right)^2, u_y = 0 \quad (17a)$$

$$y = 0 : u_x = 0, u_y = 0 \quad (17b)$$

$$y = H : u_x = 0, u_y = 0 \quad (17c)$$

$$(x, y) \in \Gamma_o : u_x = 0, u_y = 0. \quad (17d)$$

Figure 5 shows the x velocity, y velocity, and the pressure solution for the Navier Stokes equation using IBN for an aerofoil.

Parametric Steady State Heat Equation:

We revisit Poisson's equation for a family of objects characterized by boundary Γ_o . Specifically, we consider the object boundary to be taken from a set of parameterized curves. The parametrization here is a NURBS-based one. This is equivalent to having access to the point cloud representing the object. We show results for two distinct distributions of objects. The first example consists of irregularly shaped objects without obvious parametrization, while the second consists of a parametrizable family of one thousand NACA airfoils. Figure 6 shows some anecdotal example predictions of such a trained network. Each example consists of a *single trained IBN*, which is then queried for a set of unseen object boundaries. IBN can accurately predict the field solution under non-trivial geometries, as a comparison with a high-resolution FEM solver confirms (columns 3, 6, 9, 12).

Comparisons:

We compare IBN to standard FE-based result for Poisson's equation in 2D and compare it with one of the state-of-the-art methods, PINNs[7]. Table 2 shows comparison of IBN to numerical solution

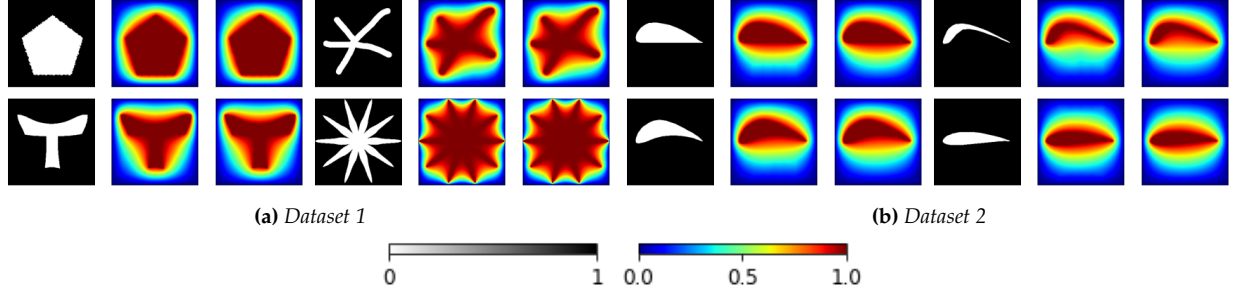


Figure 6: IBN applied on two different datasets. Within each panel: the left shows the heat source in white, the middle shows the IBN-predicted temperature distribution, and the right shows the fully converged numerical solution.

obtained using traditional approaches such as [6, 26–28]. Similarly, we show these comparisons for PINNs as well. Our approach is consistently more accurate than PINNs in predicting the field solutions. Also, the training time for PINNs is much higher than the training time for IBN. Since PINNs can deal with only one geometry at a time, we show similar training behavior, but our approach can generalize to more than one geometry.

Table 2: Comparison of L_2 norm of errors incurred by the proposed IBN method and PINN, respectively when compared with a baseline numerical solver. and timing for prediction of solution from PINNs and IBN

| Geometry | $\ u_{PINN} - u_{FEM}\ $ | $\ u_{IBN} - u_{FEM}\ $ | Training time PINN (s) | Training time IBN (s) |
|-----------|--------------------------|-------------------------|---------------------------|--------------------------|
| 2032C | 0.1638 | 0.0158 | 3667.83 | 329.35 |
| A18 | 0.1745 | 0.0156 | 3893.29 | 286.41 |
| NACA 0012 | 0.1483 | 0.0158 | 3890.78 | 245.64 |
| NACA 0010 | 0.1536 | 0.0157 | 2031.78 | 279.98 |
| NACA 0021 | 0.1471 | 0.0160 | 3666.13 | 244.36 |

Limitations:

One of the major limitations is that compared to other neural PDE solvers, our proposed approach is more memory intensive while being better and faster than them. Further, the two occupancy information calculation approaches have a trade-off. While the winding number-based approach is easier to calculate and faster, they are not robust to noise and require huge memory resources to perform the computation. Similarly, the Eikonal equation-based approach is more robust to noise in the geometry representation and has a smaller memory footprint, but suffers from a long time to compute the SDF accurately and causes initial stability issues.

6 Conclusions

We have developed a neural PDE solver that can handle irregularly shaped domains by building on well-established finite element and immersed boundary methods. Our neural PDE solver, coined IBN, demonstrates the ability to predict field solutions for irregular boundaries immersed in the target domain. We highlight two specific PDE cases, Poisson and Navier-Stokes, which show promising results. Alongside the empirical results, we have included theoretical results for the error bounds of the optimization process of our finite element-based loss function. IBN opens up fast design exploration and topology optimization for various societally critical applications such as room ventilation for reduced disease risk, shape design for energy harvesters, and aerodynamic design of vehicles.

References

- [1] Thomas JR Hughes. The finite element method: linear static and dynamic finite element analysis. Courier Corporation, 2012.
- [2] Randall J LeVeque. Finite difference methods for ordinary and partial differential equations: steady-state and time-dependent problems. SIAM, 2007.
- [3] Lloyd N Trefethen. Spectral methods in MATLAB. SIAM, 2000.
- [4] Jeffrey Slotnick, Abdollah Khodadoust, Juan Alonso, David Darmofal, William Gropp, Elizabeth Lurie, and Dimitri Mavriplis. CFD vision 2030 study: A path to revolutionary computational aerosciences. In 54th AIAA Aerospace Sciences Meeting, 2014.
- [5] Charles S Peskin. The immersed boundary method. Acta numerica, 11:479–517, 2002.
- [6] Kumar Saurabh, Boshun Gao, Milinda Fernando, Songzhe Xu, Makrand A Khanwale, Biswajit Khara, Ming-Chen Hsu, Adarsh Krishnamurthy, Hari Sundar, and Baskar Ganapathysubramanian. Industrial scale large eddy simulations with adaptive octree meshes using immersogeometric analysis. Computers & Mathematics with Applications, 97:28–44, 2021.
- [7] Maziar Raissi, Paris Perdikaris, and George E Karniadakis. Physics-informed neural networks: A deep learning framework for solving forward and inverse problems involving nonlinear partial differential equations. Journal of Computational Physics, 378:686–707, 2019.
- [8] Ehsan Kharazmi, Zhongqiang Zhang, and George Em Karniadakis. Variational physics-informed neural networks for solving partial differential equations. arXiv preprint arXiv:1912.00873, 2019.
- [9] Justin Sirignano and Konstantinos Spiliopoulos. Dgm: A deep learning algorithm for solving partial differential equations. Journal of computational physics, 375:1339–1364, 2018.
- [10] Liu Yang, Dongkun Zhang, and George Em Karniadakis. Physics-informed generative adversarial networks for stochastic differential equations. arXiv preprint arXiv:1811.02033, 2018.
- [11] Guofei Pang, Lu Lu, and George Em Karniadakis. fpinns: Fractional physics-informed neural networks. SIAM Journal on Scientific Computing, 41(4):A2603–A2626, 2019.
- [12] Sharmila Karumuri, Rohit Tripathy, Ilias Bilionis, and Jitesh Panchal. Simulator-free solution of high-dimensional stochastic elliptic partial differential equations using deep neural networks. Journal of Computational Physics, 404:109120, 2020.
- [13] Jiequn Han, Arnulf Jentzen, and E Weinan. Solving high-dimensional partial differential equations using deep learning. Proceedings of the National Academy of Sciences, 115(34):8505–8510, 2018.
- [14] Craig Michoski, Milos Milosavljevic, Todd Oliver, and David Hatch. Solving irregular and data-enriched differential equations using deep neural networks. arXiv preprint arXiv:1905.04351, 2019.
- [15] Esteban Samaniego, Cosmin Anitescu, Somdatta Goswami, Vien Minh Nguyen-Thanh, Hongwei Guo, Khader Hamdia, X Zhuang, and T Rabczuk. An energy approach to the solution of partial differential equations in computational mechanics via machine learning: Concepts, implementation and applications. Computer Methods in Applied Mechanics and Engineering, 362:112790, 2020.
- [16] Amuthan A Ramabathiran and Prabhu Ramachandran. Spinn: Sparse, physics-based, and partially interpretable neural networks for pdes. Journal of Computational Physics, 445:110600, 2021.
- [17] Lu Lu, Pengzhan Jin, and George Em Karniadakis. Deeponet: Learning nonlinear operators for identifying differential equations based on the universal approximation theorem of operators. arXiv preprint arXiv:1910.03193, 2019.
- [18] Sergio Botelho, Ameya Joshi, Biswajit Khara, Soumik Sarkar, Chinmay Hegde, Santi Adavani, and Baskar Ganapathysubramanian. Deep generative models that solve pdes: Distributed computing for training large data-free models. arXiv preprint arXiv:2007.12792, 2020.

- [19] Aditya Balu, Sergio Botelho, Biswajit Khara, Vinay Rao, Chinmay Hegde, Soumik Sarkar, Santi Adavani, Adarsh Krishnamurthy, and Baskar Ganapathysubramanian. Distributed multigrid neural solvers on megavoxel domains. arXiv preprint arXiv:2104.14538, 2021.
- [20] Nils Wandel, Michael Weinmann, Michael Neidlin, and Reinhard Klein. Spline-pinn: Approaching pdes without data using fast, physics-informed hermite-spline cnns. arXiv preprint arXiv:2109.07143, 2021.
- [21] Pola Lydia Lagari, Lefteri H Tsoukalas, Salar Safarkhani, and Isaac E Lagaris. Systematic construction of neural forms for solving partial differential equations inside rectangular domains, subject to initial, boundary and interface conditions. International Journal on Artificial Intelligence Tools, 29(05):2050009, 2020.
- [22] N Sukumar and Ankit Srivastava. Exact imposition of boundary conditions with distance functions in physics-informed deep neural networks. Computer Methods in Applied Mechanics and Engineering, 389:114333, 2022.
- [23] Rajat Mittal and Gianluca Iaccarino. Immersed boundary methods. Annu. Rev. Fluid Mech., 37:239–261, 2005.
- [24] Lucy Zhang, Axel Gerstenberger, Xiaodong Wang, and Wing Kam Liu. Immersed finite element method. Computer Methods in Applied Mechanics and Engineering, 193(21-22):2051–2067, 2004.
- [25] Fei Xu, Dominik Schillinger, David Kamensky, Vasco Varduhn, Chenglong Wang, and Ming-Chen Hsu. The tetrahedral finite cell method for fluids: Immersogeometric analysis of turbulent flow around complex geometries. Computers & Fluids, 141:135–154, 2016.
- [26] Wolfgang Bangerth, Ralf Hartmann, and Guido Kanschat. deal. ii—a general-purpose object-oriented finite element library. ACM Transactions on Mathematical Software (TOMS), 33(4):24–es, 2007.
- [27] Boyce E Griffith, Richard D Hornung, David M McQueen, and Charles S Peskin. An adaptive, formally second order accurate version of the immersed boundary method. Journal of computational physics, 223(1):10–49, 2007.
- [28] Raphael Egan, Arthur Guittet, Fernando Temprano-Colet, Tobin Isaac, François J Peaudecerf, Julien R Landel, Paolo Luzzatto-Fegiz, Carsten Burstedde, and Frederic Gibou. Direct numerical simulation of incompressible flows on parallel octree grids. Journal of Computational Physics, 428:110084, 2021.
- [29] Gavin Barill, Neil G Dickson, Ryan Schmidt, David IW Levin, and Alec Jacobson. Fast winding numbers for soups and clouds. ACM Transactions on Graphics (TOG), 37(4):1–12, 2018.
- [30] Yaron Lipman. Phase transitions, distance functions, and implicit neural representations. arXiv, 2021. doi: 10.48550/ARXIV.2106.07689. URL <https://arxiv.org/abs/2106.07689>.
- [31] Alexandre Ern and Jean-Luc Guermond. Finite Elements II: Galerkin Approximation, Elliptic and Mixed PDEs, volume 73. Springer Nature, 2021.
- [32] Dominik Schillinger, Isaac Harari, Ming-Chen Hsu, David Kamensky, Stein KF Stoter, Yue Yu, and Ying Zhao. The non-symmetric nitsche method for the parameter-free imposition of weak boundary and coupling conditions in immersed finite elements. Computer Methods in Applied Mechanics and Engineering, 309:625–652, 2016.
- [33] Aladin Virmaux and Kevin Scaman. Lipschitz regularity of deep neural networks: analysis and efficient estimation. Advances in Neural Information Processing Systems, 31, 2018.
- [34] Mats G Larson and Fredrik Bengzon. The finite element method: theory, implementation, and applications, volume 10. Springer Science & Business Media, 2013.
- [35] Alex Main and Guglielmo Scovazzi. The shifted boundary method for embedded domain computations. part i: Poisson and stokes problems. Journal of Computational Physics, 372:972–995, 2018.

- [36] Anita Hansbo and Peter Hansbo. An unfitted finite element method, based on nitsche’s method, for elliptic interface problems. Computer methods in applied mechanics and engineering, 191(47-48): 5537–5552, 2002.
- [37] Léon Bottou. Stochastic gradient descent tricks. In Neural networks: Tricks of the trade, pages 421–436. Springer, 2012.
- [38] Chaoyue Liu, Libin Zhu, and Mikhail Belkin. Loss landscapes and optimization in over-parameterized non-linear systems and neural networks. Applied and Computational Harmonic Analysis, 2022.
- [39] Hamed Karimi, Julie Nutini, and Mark Schmidt. Linear convergence of gradient and proximal-gradient methods under the polyak-łojasiewicz condition. In Joint European Conference on Machine Learning and Knowledge Discovery in Databases, pages 795–811. Springer, 2016.
- [40] Robert Mansel Gower, Nicolas Loizou, Xun Qian, Alibek Sailanbayev, Egor Shulgin, and Peter Richtárik. Sgd: General analysis and improved rates. In International Conference on Machine Learning, pages 5200–5209. PMLR, 2019.
- [41] Léon Bottou, Frank E Curtis, and Jorge Nocedal. Optimization methods for large-scale machine learning. Siam Review, 60(2):223–311, 2018.
- [42] Onur Rauf Bingol and Adarsh Krishnamurthy. NURBS-Python: An open-source object-oriented NURBS modeling framework in Python. SoftwareX, 9:85–94, 2019. doi: <https://doi.org/10.1016/j.softx.2018.12.005>.

Appendix

A Theory for Generalization Error

In this section, we show in detail the convergence behavior of the generalization error for IBN. For a given surface of the geometry, Γ_o and let u^h be the discrete optimum solution to the PDE, evaluated at any point $\underline{x} \in \Omega$. Note that, u^h need not be the optimum solution to the PDE itself and we denote u as the original optimum solution to the PDE. Hence, $\|u^h - u\|$ is a known error due to the discretization of Ω_B . We will have more discussion about this later in this section.

Now, given the discrete optimum solution u^h predicted by the network $G(\{P\}, \theta)$, we can express the generalization error e_G as follows:

$$\|e_G^k\| = \|u_{\theta_k} - u\| = \|u_{\theta_k} - u_{\theta^*} + u_{\theta^*} - u^h + u^h - u\| \quad (10)$$

where, u_{θ_k} is the field solutions corresponding to the network parameters θ_k at k^{th} iteration of the optimization and u_{θ^*} is the theoretical optimum of u_{θ_k} that an algorithm can achieve ideally.

To follow the convention in optimization domain, we analyze the quadratic form of $\|e_G^k\|$, i.e., $\|e_G^k\|^2$, and in a stochastic setting, it is equivalent to the second moment, i.e., $\mathbb{E}[\|e_G^k\|^2]$. By applying a fundamental inequality $\|a + b + c\|^2 \leq 3(\|a\|^2 + \|b\|^2 + \|c\|^2)$, we can obtain

$$\|e_G^k\|^2 \leq 3 \left(\underbrace{\|u_{\theta_k} - u_{\theta^*}\|^2}_{\text{Optimization error}} + \underbrace{\|u_{\theta^*} - u^h\|^2}_{\text{Modeling error}} + \underbrace{\|u^h - u\|^2}_{\text{Discretization error}} \right). \quad (11)$$

Thus the generalization error is bounded above by three different terms, which are respectively the *optimization error*, *modeling error*, and *discretization error*. The discretization error is only dependent on the choice of the discretization and the modeling error is based on the choice of the network architecture and hence both the errors remains static through out the optimization.

To facilitate the understanding of how $\|e_G^k\|^2$ converges and to simplify the analysis, we will next combine the optimization error and modeling error, while following standard analysis techniques from numerical analysis for the discretization error. To achieve that, the following assumption is required.

Assumption 1. There exists a constant $c > 0$ such that $\|u_{\theta^*} - u^h\| \leq c\|u_{\theta_k} - u_{\theta^*}\|, \forall k \geq 0$.

Assumption 1 implies that the modeling error can be upper bounded by the optimization error up to a constant. As the modeling error is determined by two categories of optima, this intuitively makes sense since we can always find some constant c to let the above assumption hold. c could be large when u_{θ_k} is close to u_{θ^*} . While in practice an approximate solution for u_{θ^*} is typically sufficient such that $c < \infty$. Thus, we now have

$$\|e_G^k\|^2 \leq 3[(1 + c^2)\|u_{\theta_k} - u_{\theta^*}\|^2 + \|u^h - u\|^2]. \quad (12)$$

Now the problem is to find the bounds for the two terms on the right hand side of [Equation 12](#).

Since the solution function u^h has been parameterized by θ , to obtain the upper bound for the generalization error, we need to establish the relationship between $\|u_{\theta_k} - u_{\theta^*}\|$ and $\|\theta_k - \theta^*\|$. Recall

the following equations:

$$u_{\theta_k} := u^h(\mathbf{x}; \theta_k) = \sum_{i=1}^N \mathcal{B}_i(\mathbf{x}) U_i(\theta_k) \quad (18a)$$

$$u^* := u^h(\mathbf{x}; \theta^*) = \sum_{i=1}^N \mathcal{B}_i(\mathbf{x}) U_i(\theta^*) \quad (18b)$$

Using the last two equations yields

$$\begin{aligned} \|u_{\theta_k} - u_{\theta^*}\| &= \left\| \sum_{i=1}^N \mathcal{B}_i(\mathbf{x}) U_i(\theta_k) - \sum_{i=1}^N \mathcal{B}_i(\mathbf{x}) U_i(\theta^*) \right\| \\ &= \left\| \sum_{i=1}^N \mathcal{B}_i(\mathbf{x}) (U_i(\theta_k) - U_i(\theta^*)) \right\| \\ &\leq \sum_{i=1}^N \|\mathcal{B}_i(\mathbf{x}) U_i(\theta_k) - \mathcal{B}_i(\mathbf{x}) U_i(\theta^*)\| \\ &\leq \sum_{i=1}^N \|\mathcal{B}_i(\mathbf{x})\| \|U_i(\theta_k) - U_i(\theta^*)\|, \end{aligned} \quad (19)$$

where the first inequality follows the triangle inequality and the second Cauchy-Schwartz inequality. As the nodal value function $U_i(\cdot)$ is parameterized by the weights θ , in the optimization area, there exists generic assumption on its Lipschitz continuity. One may argue that this may not be practically feasible during implementation, but a regularization can be added to make it true. For simplicity, we impose it in the following directly:

Assumption 2. There exists a constant $L > 0$ such that for all $x, y \in \mathbb{R}^d$, $\|U_i(x) - U_i(y)\| \leq L\|x - y\|$, for all $i \in \{1, 2, \dots, N\}$.

Hence, Eq. 19 can be rewritten as

$$\|u_{\theta_k} - u_{\theta^*}\| \leq L \leq \sum_{i=1}^N \|\mathcal{B}_i(\mathbf{x})\| \|\theta_k - \theta^*\|, \quad (20)$$

where θ^* is the theoretical optimum of weights. Combining the last inequality with Eq. 12 yields

$$\begin{aligned} \|e_G^k\|^2 &\leq 3[(1 + c^2)L^2 \left(\sum_{i=1}^N \|\mathcal{B}_i(\mathbf{x})\| \|\theta_k - \theta^*\| \right)^2 + \|u^h - u\|^2] \\ &\leq 3[(1 + c^2)L^2 N \sum_{i=1}^N \|\mathcal{B}_i(\mathbf{x})\|^2 \|\theta_k - \theta^*\|^2 + \|u^h - u\|^2], \end{aligned} \quad (21)$$

where the second inequality follows from that $(\sum_{i=1}^N \|a_i\|)^2 \leq N \sum_{i=1}^N \|a_i\|^2$. As the basis function $\mathcal{B}_i(\cdot)$ is a bounded function, we denote by $\hat{\mathcal{B}}$ the upper bound over all i . Hence, Eq. 21 is rewritten as

$$\|e_G^k\|^2 \leq 3[(1 + c^2)L^2 N^2 \hat{\mathcal{B}}^2 \|\theta_k - \theta^*\|^2 + \|u^h - u\|^2]. \quad (22)$$

Remark 3. We remark why the stochastic optimization theory can be applied in this context to study the convergence behavior of the IBN. As will be presented in the latter sections, some assumptions will be imposed on the \mathcal{J} . However, in the PDE domain, such assumptions may not be practically

feasible. It should be noted that though the application focused is PDE, the functions have been *parameterized* such that the property of loss \mathcal{J} is similar as in the machine learning (even deep learning)-based optimization problems. Additionally, the algorithm we leverage to search for the optimal weights are the popular gradient descent type. These motivate us to study the convergence rate in this work, following some similar assumptions adopted in the stochastic optimization literature.

Remark 4. In this work, the analysis for the generalization error is based on the gradient descent type of algorithms. While there are other types of popular algorithms, such as accelerated or adaptive gradient descent, (stochastic) gradient descent remains the most fundamental one. Thus, this is the first step to facilitate the understanding of different errors in the PDE domain. Note, however that, for the implementation, other algorithms can be adopted, and we envision that the (stochastic) gradient descent algorithm may not perform the best empirically. Another aspect we would like to point out is that though due to different algorithms, the explicit error bounds vary, but the convergence rate can still be similar.

A.1 An Ideal Bound

We first investigate the convergence rate when \mathcal{J} is *strongly convex and in a batch setting*. Via Eq. 8, it can be seen that the two terms for boundary condition and exterior points are quadratic, which play a role as regularizers, turning the whole loss strongly convex if the first term of PDE loss is convex. While this scenario is typically not practical in the real implementation, it will show us the convergence behavior and an ideal bound that can deliver meaningful insights in terms of optimality and generalization error. To characterize the first main result, we present two well-known lemmas as follows.

Lemma 5. *If a continuously differentiable function $f : \mathbb{R}^d \rightarrow \mathbb{R}$ is μ -strongly convex, for all $x, y \in \mathbb{R}^d$, then*

$$\langle \nabla f(x) - \nabla f(y), x - y \rangle \geq \mu \|x - y\|^2. \quad (23)$$

Lemma 6. *If a continuously differentiable function $f : \mathbb{R}^d \rightarrow \mathbb{R}$ is μ -strongly convex and β -smooth, for all $x, y \in \mathbb{R}^d$, then*

$$\langle \nabla f(x) - \nabla f(y), x - y \rangle \geq \frac{\mu\beta}{\mu + \beta} \|x - y\|^2 + \frac{1}{\mu + \beta} \|\nabla f(x) - \nabla f(y)\|^2. \quad (24)$$

With these two lemma in hand, we are now ready to present a key auxiliary lemma.

Lemma 7. *Suppose that \mathcal{J} is μ -strongly convex and β -smooth. By applying the gradient descent algorithm with a constant step size $\eta_k = \eta = \frac{2}{\mu + \beta}$, the iterates $\{\theta_k\}$ satisfy the following relationship*

$$\|\theta_K - \theta^*\|^2 \leq \left(1 - \frac{2}{\kappa + 1}\right)^{2K} \|\theta_0 - \theta^*\|^2, \quad (25)$$

where $\kappa = \frac{\beta}{\mu} \geq 1$ and K is the number of epochs.

Proof. Based on the gradient descent update, we have

$$\begin{aligned}
\|\theta_k - \theta^*\|^2 &= \|\theta_{k-1} - \eta \nabla \mathcal{J}(\theta_{k-1}) - \theta^*\|^2 \\
&= \|\theta_{k-1} - \theta^*\|^2 - 2\eta \langle \nabla \mathcal{J}(\theta_{k-1}), \theta_{k-1} - \theta^* \rangle + \eta^2 \|\nabla \mathcal{J}(\theta_{k-1})\|^2 \\
&\leq \left(1 - 2\frac{\mu\beta\eta}{\mu + \beta}\right) \|\theta_{k-1} - \theta^*\|^2 + \left(\eta^2 - \frac{2\gamma}{\mu + \beta}\right) \|\nabla \mathcal{J}(\theta_{k-1})\|^2 \\
&= \left(1 - \frac{2}{\kappa + 1}\right)^2 \|\theta_{k-1} - \theta^*\|^2 \\
&\leq \left(1 - \frac{2}{\kappa + 1}\right)^{2k} \|\theta_0 - \theta^*\|^2.
\end{aligned} \tag{26}$$

The first inequality follows from the substitution of the step size and Lemma 6. While the third equality is due to $\eta^2 - \frac{2\gamma}{\mu + \beta} = 0$. The desirable result is obtained by changing k to K . \square

Lemma 7 implies the upper bound of $\|\theta_K - \theta^*\|^2$ and shows the *linear* convergence rate with a constant $\rho_1 = \left(1 - \frac{2}{\kappa + 1}\right)^2$. Intuitively, the convergence to θ^* is quite fast based on the above result, particularly when the initialization θ_0 is close to θ^* . That said, if the loss induced by the IBN is approximately strongly convex, and smooth, the optimization error decays in a linear rate in a batch setting, which is summarized in the following. Before that, we present another lemma that shows the upper bound of the discretization error $\|u^h - u\|^2$.

Lemma 8. *Assume that the basis function $\mathcal{B}_i(\mathbf{x})$ are chosen such that they are at least continuously differentiable locally over a mesh. Then the following relationship holds true:*

$$\|u^h - u\|^2 \leq Ch^{2\alpha}, \tag{27}$$

where $C > 0$ and α is the order of continuous derivative. Typically, $\alpha \geq 1$.

The proof follows an analysis similar to that presented in [31, 35, 36]. Lemma 8 states the static property of the discretization error, and implies that the decaying of the error is bounded by the second order of the resolution h . This observation is critical as the number of basis functions N has a relationship with h such that a tradeoff between the optimization error and discretization error can be found. More detail will be shown in the latter analysis. We are now ready to present the first main result.

Theorem 9. Suppose that \mathcal{J} is μ -strongly convex and β -smooth. Let Assumptions 1 and 2 hold. By applying the gradient descent algorithm with a constant step size $\eta_k = \eta = \frac{2}{\mu + \beta}$, the generalization error $\|e_G^K\|^2$ satisfies the following relationship after K epochs,

$$\|e_G^K\|^2 \leq 3(1 + c^2)L^2N^2\hat{\mathcal{B}}^2 \left(1 - \frac{2}{\kappa + 1}\right)^{2K} \|\theta_0 - \theta^*\|^2 + 3Ch^{2\alpha}. \tag{28}$$

Proof. The desirable result can immediately be obtained by combining Eqs. 22, 25, and 27. \square

Theorem 9 implies that the generalization error of IBN is upper bounded by two terms, while the first one is tightly related to the optimization error caused by numerically searching for the optimal

weights and the second one shows the static error due to the discretization. Additionally, in an asymptotic manner, we have that

$$\lim_{K \rightarrow \infty} \|e_G^K\|^2 \leq 3Ch^{2\alpha}, \quad (29)$$

which suggests that the generalization error will ultimately be dominated by the discretization error determined by the resolution h and the order α , both of which rely on the definition of basis functions $\{\mathcal{B}_i(\mathbf{x})\}_{i=1}^N$. According to the domain knowledge [34], the resolution h is a function of the number of basis functions, resulting in $h \propto \frac{1}{\sqrt{N}}$ (due to the 2D analysis in this context). With this relationship, if h is chosen such that $h = \mathcal{O}(\frac{1}{\sqrt{KN}})$, the following corollary can be obtained:

Corollary 10. *Suppose that $h = \mathcal{O}(\frac{1}{\sqrt{KN}})$. Given all conditions and parameters from Theorem 9, the generalization error achieves an overall sublinear convergence rate*

$$\|e_G^K\|^2 \leq \mathcal{O}\left(N^2\rho_1^K + \frac{1}{(NK)^\alpha}\right). \quad (30)$$

A quick observation is that the generalization error depends primarily on the number of basis functions N and the number of epochs K . Though Corollary 10 implies a satisfactory convergence rate, it requires strong conditions such as batch setting and strongly convex loss. While, surprisingly, with an explicit relationship between h and N in the error bound, it shows a clear *tradeoff* between the optimization error and discretization error such that a smaller N can lead to an easier optimization procedure but causing larger discretization error. Such a result can also help practitioners in the practical design for selecting the (nearly) optimal N or h . In the following, we will make attempts to relax the conditions for either the setting or loss function and verify if such a tradeoff is still existing.

A.2 Stochastic Setting & Polyak-Lojasiewicz Condition

In a batch setting, the computational overhead could be an issue when the number of data points is significantly large. Thus, stochastic gradient descent (SGD) [37] has been one of the most popular optimization algorithms. Further, the loss functions associated with most real-world problems are not necessarily strongly convex. In Eq. 8, the loss consists of three terms and the last two terms are strongly convex, while the property of the first term can determine the property of the whole loss. In this section, we present the theoretical analysis for the generalization error e_G^K with the stochastic setting, and the loss satisfies a relaxed condition, termed *Polyak-Lojasiewicz (PL) condition*, which complies more with the practical implementation and has been provably shown to hold across most of the parameter space in over-parameterized networks [38]. It has been acknowledged that the strong convexity implies PL condition, but not vice versa, as the loss can possibly be *non-convex*. When applying SGD, the sampling technique is adopted for calculating the gradients such that they are *noisy*. Popular random sampling techniques such as uniform sampling $\mathcal{U}(\{1, \dots, N_s\})$ have been used widely. This motivates us to define a σ -field for each time step k , i.e., $\mathcal{F}_k = \sigma(I_0, \dots, I_k)$, where $\mathcal{F}_{-1} = \{\Omega, \emptyset\}$, and $I_k \sim \mathcal{U}(\{1, \dots, N_s\})$ indicates each realization of random sampling. It is noted that θ_k is \mathcal{F}_{k-1} -measurable, i.e., θ_k only depends on I_0, \dots, I_{k-1} . Based on the defined setting here, one well-known result is that a stochastic gradient is an independent and unbiased estimate of the gradient $\mathbb{E}[\nabla \mathcal{J}_{I_k}(\theta_k) | \mathcal{F}_{k-1}] = \nabla \mathcal{J}(\theta_k)$. Due to the stochasticity, Eq. 22 is now rewritten by taking expectation on both sides

$$\mathbb{E}[\|e_G^K\|^2 | \mathcal{F}_{k-1}] \leq 3[(1+c^2)L^2N^2\hat{\mathcal{B}}^2\mathbb{E}[\|\theta_k - \theta^*\|^2 | \mathcal{F}_{k-1}] + \|u^h - u\|^2]. \quad (31)$$

Similarly, to obtain the upper bound for $\mathbb{E}[\|e_G^k\|^2|\mathcal{F}_{k-1}]$, the key is to investigate the upper bound of $\mathbb{E}[\|\theta_k - \theta^*\|^2|\mathcal{F}_{k-1}]$, which is shown in the next auxiliary lemma, adapted from [39]. We first present the PL inequality in the following.

$$\frac{1}{2}\|\nabla\mathcal{J}(\theta)\|^2 \geq \mu(\mathcal{J}(\theta) - \mathcal{J}(\theta^*)), \forall\theta. \quad (32)$$

Intuitively, this inequality suggests that the gradient grows faster than a quadratic function as it moves away from the optimal function value. Also, every stationary point is a global optimum when the loss satisfies this condition. This differs from the strong convexity, which implies a unique solution.

Lemma 11. *Let $(\mathcal{F}_k)_k$ be an increasing family of σ -fields. For each $k \geq 0$, suppose that \mathcal{J} is a β -smooth, differentiable, and \mathcal{F}_k -measurable function over Θ . Also, assume that $\mathbb{E}[\nabla\mathcal{J}_{I_k}(\theta_k)|\mathcal{F}_{k-1}] = \nabla\mathcal{J}(\theta_k)$, for each $\theta \in \Theta$ and $k \geq 1$, where \mathcal{J} satisfies the μ -PL condition. If $\forall k \geq 0$, $\mathbb{E}[\|\nabla\mathcal{J}_{I_k}(\theta_k)\|^2|\mathcal{F}_{k-1}] \leq \sigma^2$, then the iterates $\{\theta_k\}$ satisfy the following relationship after K epochs,*

$$\mathbb{E}[\|\theta_K - \theta^*\|^2] \leq (1 - 2\mu\eta)^{K-1} \frac{2[\mathcal{J}(\theta_0) - \mathcal{J}(\theta^*)]}{\mu} + \frac{\beta\sigma^2\eta}{2\mu^2}, \quad (33)$$

when the step size $\eta_k = \eta < \frac{1}{2\mu}$.

Based on the update from the SGD, and the definition of β -smooth, we have the following relationship

$$\mathcal{J}(\theta_{k+1}) \leq \mathcal{J}(\theta_k) - \eta_k \langle \nabla\mathcal{J}(\theta_k), \nabla\mathcal{J}_{I_{k+1}}(\theta_k) \rangle + \frac{\beta\eta_k^2}{2} \|\nabla\mathcal{J}_{I_{k+1}}(\theta_k)\|^2. \quad (34)$$

Taking the expectation for both sides w.r.t. I_{k+1} yields

$$\begin{aligned} \mathbb{E}[\mathcal{J}(\theta_{k+1})|\mathcal{F}_k] &\leq \mathcal{J}(\theta_k) - \eta_k \langle \nabla\mathcal{J}(\theta_k), \mathbb{E}[\nabla\mathcal{J}_{I_{k+1}}(\theta_k)|\mathcal{F}_k] \rangle + \frac{\beta\eta_k^2}{2} \mathbb{E}[\|\nabla\mathcal{J}_{I_{k+1}}(\theta_k)\|^2|\mathcal{F}_k] \\ &\leq \mathcal{J}(\theta_k) - \eta_k \|\nabla\mathcal{J}(\theta_k)\|^2 + \frac{\beta\sigma^2\eta_k^2}{2} \\ &\leq \mathcal{J}(\theta_k) - 2\mu\eta_k(\mathcal{J}(\theta_k) - \mathcal{J}(\theta^*)) + \frac{\beta\sigma^2\eta_k^2}{2}, \end{aligned} \quad (35)$$

where the second inequality follows from the unbiased estimate of a stochastic gradient and the bounded second moment, the third inequality follows from the PL condition. Subtracting $\mathcal{J}(\theta^*)$ on both sides leads to the following inequality

$$\mathbb{E}[\mathcal{J}(\theta_{k+1}) - \mathcal{J}(\theta^*)|\mathcal{F}_k] \leq (1 - 2\mu\eta_k)(\mathcal{J}(\theta_k) - \mathcal{J}(\theta^*)) + \frac{\beta\sigma^2\eta_k^2}{2}. \quad (36)$$

As $\eta_k = \eta < \frac{1}{2\mu}$, by applying the last inequality recursively, the following can be obtained

$$\begin{aligned} \mathbb{E}[\mathcal{J}(\theta_{k+1}) - \mathcal{J}(\theta^*)|\mathcal{F}_k] &\leq (1 - 2\mu\eta)^k (\mathcal{J}(\theta_0) - \mathcal{J}(\theta^*)) + \frac{\beta\sigma^2\eta^2}{2} \sum_{j=0}^k (1 - 2\mu\eta)^j \\ &\leq (1 - 2\mu\eta)^k (\mathcal{J}(\theta_0) - \mathcal{J}(\theta^*)) + \frac{\beta\sigma^2\eta^2}{2} \sum_{j=0}^{\infty} (1 - 2\mu\eta)^j \\ &\leq (1 - 2\mu\eta)^k (\mathcal{J}(\theta_0) - \mathcal{J}(\theta^*)) + \frac{\beta\sigma^2\eta}{4\mu}. \end{aligned} \quad (37)$$

The last inequality follows the definition of step size and the property of the geometric series. As the PL condition implies the *quadratic growth* property [39], which suggests

$$\mathcal{J}(\theta) - \mathcal{J}(\theta^*) \geq \frac{\mu}{2} \|\theta - \theta^*\|^2. \quad (38)$$

Thus, combining the last two inequalities and replacing k with K completes the proof.

Lemma 11 shows that with a constant step size η , θ_k will converge linearly to the neighborhood of θ^* , up to a constant w.r.t. η and σ^2 . This indicates the impact of the noisy stochastic gradient, while we can reduce it by selecting a smaller step size, which, however, would increase $1 - 2\mu\eta$, resulting in slower convergence.

It is ready to state the following main result for the generalization error in the stochastic setting with the PL condition.

Theorem 12. Given all conditions and parameters defined in Lemma 11 and let Assumptions 1 and 2 hold. Then the generalization error $\mathbb{E}[\|e_G^K\|^2]$ satisfies the following relationship after K epochs,

$$\mathbb{E}[\|e_G^K\|^2] \leq 3(1 + c^2)L^2N^2\hat{\mathcal{B}}^2 \left((1 - 2\mu\eta)^{K-1} \frac{2[\mathcal{J}(\theta_0) - \mathcal{J}(\theta^*)]}{\mu} + \frac{\beta\sigma^2\eta}{2\mu^2} \right) + 3Ch^{2\alpha}. \quad (39)$$

Proof. Combining Eq. 31, Lemma 8 and Lemma 11 immediately yields the above result. \square

We now analyze the error bound in this context. Inherently, the optimization error is directly impacted by the updates of weight parameters from Lemma 11 such that in an asymptotic manner, the generalization error converges to a constant involving both optimization error and discretization error eventually, i.e.,

$$\lim_{K \rightarrow \infty} \mathbb{E}[\|e_G^K\|^2] \leq 3(1 + c^2)L^2N^2\hat{\mathcal{B}}^2 \frac{\beta\sigma^2\eta}{2\mu^2} + 3Ch^{2\alpha}.$$

Compared to Theorem 9, the asymptotic error is larger due to the stochastic gradient noise term $\frac{\beta\sigma^2\eta}{2\mu^2}$, which can be enlarged by the number of basis functions N . This may suggest a relative worse minimum, which has also been shown in previous works [40, 41]. As discussed above, one can leverage the step size to control its negative impact, while this also affects the convergence of the optimization procedure. The discretization error remains the same because of its static nature. Similarly, when we apply the same relationship between N and h , the following corollary summarizes the result in a noisy environment.

Corollary 13. Suppose that $h = \mathcal{O}(\frac{1}{\sqrt{KN}})$. Given all conditions and parameters defined in Theorem 12, the generalization error enjoys a sublinear convergence rate and converges to a neighborhood of the minimum up to a constant w.r.t. $N^2\sigma^2$,

$$\mathbb{E}[\|e_G^K\|^2] \leq \mathcal{O} \left(N^2\rho_2^K + N^2\sigma^2 + \frac{1}{(NK)^\alpha} \right), \quad (40)$$

where $\rho_2 = (1 - 2\mu\eta)$.

Similar to Corollary 10, an immediate observation from Corollary 13 is that the error bound still involves the clear tradeoff between the optimization error and discretization error. However, a surprising difference is that the optimization error dominates the generalization error instead

of discretization error in Corollary 10 when K is sufficiently large, as the constant term $N^2\sigma^2$ exists. Additionally, this result may imply a relatively higher overfitting than that in the batching setting due to larger optimization error. Apparently, the careful design of N is able to alleviate the overfitting phenomenon. To reduce the uncertainties brought by the noisy gradients, a decay step size needs to be adopted, instead of a constant one, while this results in a worse sublinear convergence rate for the optimization error itself. Hence, we select a decaying step size for the eliminate the effect of the noisy gradient in the optimization error.

Let the step size $\eta_k = \frac{2k+1}{2\mu(k+1)^2}$. The following lemma describes how the weight parameters evolve accordingly.

Lemma 14. *Let $(\mathcal{F}_k)_k$ be an increasing family of σ -fields. For each $k \geq 0$, suppose that \mathcal{J} is a β -smooth, differentiable, and \mathcal{F}_k -measurable function over Θ . Also, assume that $\mathbb{E}[\nabla \mathcal{J}_{I_k}(\theta_k) | \mathcal{F}_{k-1}] = \nabla \mathcal{J}(\theta_k)$, for each $\theta \in \Theta$ and $k \geq 1$, where \mathcal{J} satisfies the μ -PL condition. If $\forall k \geq 0$, $\mathbb{E}[\|\nabla \mathcal{J}_{I_k}(\theta_k)\|^2 | \mathcal{F}_{k-1}] \leq \sigma^2$, then the iterates $\{\theta_k\}$ satisfy the following relationship after K epochs,*

$$\mathbb{E}[\|\theta_K - \theta^*\|^2] \leq \frac{\beta\sigma^2}{K\mu^3}, \quad (41)$$

when the step size $\eta_k = \frac{2k+1}{2\mu(k+1)^2}$.

Proof. Recalling Eq. 36 and applying the step size $\eta_k = \frac{2k+1}{2\mu(k+1)^2}$ to it results in

$$\mathbb{E}[\mathcal{J}(\theta_{k+1}) - \mathcal{J}(\theta^*) | \mathcal{F}_k] \leq \frac{k^2}{(k+1)^2} (\mathcal{J}(\theta_k) - \mathcal{J}(\theta^*)) + \frac{\beta\sigma^2(2k+1)^2}{8\mu^2(k+1)^4}. \quad (42)$$

We now multiply both sides by $(k+1)^2$ and denote $\zeta_k := k^2\mathbb{E}[\mathcal{J}(\theta_k) - \mathcal{J}(\theta^*)]$ such that

$$\zeta_{k+1} \leq \zeta_k + \frac{\beta\sigma^2(2k+1)^2}{8\mu^2(k+1)^4} \leq \zeta_k + \frac{\beta\sigma^2}{2\mu^2}, \quad (43)$$

where the second inequality uses the fact that $\frac{2k+1}{k+1} < 2$. Summing up the last inequality from 0 to k and using the fact that $\zeta_0 = 0$ we can obtain the following relationship

$$\zeta_{k+1} \leq \zeta_0 + (k+1) \frac{\beta\sigma^2}{2\mu^2} = (k+1) \frac{\beta\sigma^2}{2\mu^2}. \quad (44)$$

Applying the last inequality to K and adopting the quadratic growth property in Eq. 38 completes the proof. \square

When $K \rightarrow \infty$, a diminishing step size will eliminate the negative impact of σ^2 to enable the convergence to θ^* , while at cost of the convergence rate. If defining a condition number as $\frac{\beta}{\mu}$, we can observe that a smaller condition number enables a better solution given a finite K in practice. With this in hand, the generalization error bound is obtained as follows.

Theorem 15. Given all conditions and parameters defined in Lemma 14 and let Assumptions 1 and 2 hold. Then, the generalization error $\mathbb{E}[\|e_G^K\|^2]$ satisfies the following relationship after K epochs,

$$\mathbb{E}[\|e_G^K\|^2] \leq 3(1+c^2)L^2N^2\hat{\mathcal{B}}^2 \frac{\beta\sigma^2}{K\mu^3} + 3Ch^{2\alpha}. \quad (45)$$

Proof. The proof follows from the combination among Eq. 31, Lemma 8 and Lemma 14. \square

Theorem 15 renders a similar asymptotic behavior as seen in Theorem 9, that said, the generalization error will end up with the discretization error when $K \rightarrow \infty$, but with a slower convergence rate $\mathcal{O}(\frac{1}{K})$, regardless of the noise brought by stochastic gradients. Now the following corollary summarizes the convergence rate given the explicit relationship between h and N .

Corollary 16. *Suppose that $h = \mathcal{O}(\frac{1}{\sqrt{KN}})$. Given all conditions and parameters defined in Theorem 15, the generalization error enjoys a sublinear convergence rate as follows*

$$\mathbb{E}[\|e_K^G\|^2] \leq \mathcal{O}\left(\frac{N^2}{K} + \frac{1}{(NK)^\alpha}\right). \quad (46)$$

Corollary 16 still enjoys the tradeoff between the optimization error and discretization error, while the rate is determined primarily by the former, given a sufficiently large K . This observation is different from what we have found in Corollary 10, where no noise in gradient needs to be taken into account. Hence, dealing with noisy gradients motivates us to leverage different step sizes in various scenarios. Additionally, when $\alpha = 1$, the convergence rate is $\mathcal{O}(1/K)$.

Remark 17. To summarize, through the investigations on the generalization error by using the optimization theory, we have clearly found that there exists tradeoff between optimization error and discretization error and that depending on different scenarios, either of them determines the primary convergence rate, after a sufficiently large number of epochs and given a reasonable explicit relationship among h , N and K . This initially fills in the gap between theory and practice in the parametric PDE domain. Though the properties of the loss in this work may not necessarily be practical in the real-world problem, our analysis delivers some useful and meaningful theoretical insights to the community and points out a research direction that other researchers can work on. Perhaps the more generic case for the loss is non-convex without the PL condition, while we leave this as one of our future work as the accuracy metric for the weights could be significantly from what we have used here, i.e., $\|\theta_k - \theta^*\|^2$, and it can definitely affect the definition of the generalization error.

B Additional Implementation Details

Network Architecture

The neural network architecture G mainly comprises 2D and 3D transpose convolution operations. The dimensionality of the transpose convolution operation will match the dimensionality of the domain we are solving for. We use transpose convolutions as a trainable up-sampling scheme. This is favored compared to deterministic methods such as interpolation-based upsampling methods or unpooling operations due to the added learning capacity transpose convolutions offer. The kernel size of the transpose convolution operation is initialized to encapsulate information from a neighborhood of NURBS control points.

Application of Boundary Conditions

We can accurately apply the boundary conditions to arbitrary complex domains. We accomplish this by learning the in-out function associated with a given boundary. We optimize our network to learn the in-out function using a differentiable winding numbers loss function outlined in detail below. The optimized in-out function approximation sets the elements inside the boundary to 1 and outside the boundary to 0. The inside of the object also inherits the conditions at its boundary; therefore,

the Dirichlet condition is applied to all the points in the background mesh assigned a positive winding number, along with the points on the object surface. The nodes assigned zero values are understood to belong to the computational domain, thus being used for further computations. This is accomplished with a `torch.where()` function. We then apply this processed in-out prediction as the boundary condition to the predicted field solution using a similar `torch.where()` function.

Differentiation and Integration:

The computation of the loss function \mathcal{J} in Equation 8 requires an integration of the term $v^h[\mathcal{N}(w^h) - f]$ over Ω_B . And the evaluation of $\mathcal{N}(w^h)$ in turn requires some differentiation (recall that $\mathcal{N}(\cdot)$ is a differential operator; also compare Equation 2 and Equation 3). But, this differentiation is not to be confused with the differentiation through the neural network. Rather, this derivative calculation is done using the basis functions $\{\mathcal{B}_i(\underline{x})\}_{i=1}^N$ and therefore the neural network is not responsible this.

Finally, the integration is performed numerically using Gaussian quadratures. For a given mesh \mathcal{K}^h , the basis functions $\{\mathcal{B}_i\}$ as well as the quadrature points are known and are completely deterministic. This allows us to define the spatial gradients of the predicted field solution by simply evaluating each element with the first or second-order derivative of the basis function originally used to evaluate the predicted field solution. Since we use the FEM, we perform the integration in each discrete element and then perform a summation over the finite set of elements to obtain the total integral.

Dataset Generation:

In this work we used a dataset consisting of point clouds, and the corresponding normals, which outline Non-Uniform Rational B-Splines (NURBS) curves to represent the boundaries of irregular domains. NURBS curves are presented by a set of control points, with each control point being described by cartesian coordinates, in this case only (x,y) . For this dataset, we selected points along the x-axis which were uniformly spaced from 0 to 1. The corresponding coordinates along the y-axis were randomly sampled from a uniform distribution with a minimum value of 0.2 and a maximum value of 0.8. To attain the point cloud on the boundary defined by the NURBS curve we utilized NURBS-Python[42], a geometric modeling library. NURBS-Python not only provides a point cloud on the boundary of the NURBS curve, but also the normals, unique vectors for each point in the point cloud pointing in the orthogonal direction with respect to the boundary. Additionally, the area for each point is required for the calculation of the winding number. In this work we assume each point has a uniform area, which we maintain for each irregular boundary in the entire dataset.

Differentiable Winding Number Computation:

As explained in the main paper, winding number for a given point cloud \mathcal{P} at a given query point \mathbf{q} can be computed as

$$\chi_w(\mathbf{q}) = \sum_{i=1}^m a_i \frac{(\mathbf{p}_i - \mathbf{q}) \cdot \hat{\mathbf{n}}_i}{4\pi \|\mathbf{p}_i - \mathbf{q}\|^3} \quad (47)$$

In order to evaluate the winding number at all the nodal locations, we perform all the pairwise distance computations between every nodal location and every point in the pointcloud and perform a sum reduction of the pairwise distances as per the above equation. Using `pytorch`, we can achieve this with a simple broadcasting operation. This way, all the operations are performed using the GPUs very quickly.

During experimentation, we demonstrated two different methods of generating masks to impose the boundary conditions on our predicted field solution during the Finite Element loss computation. The first was with a differentiable winding number method. The second leverages the Finite

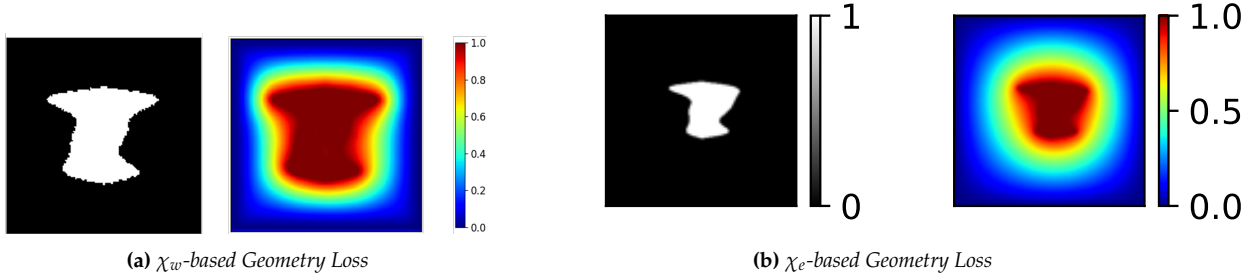


Figure 7: (a) Left: The in-out information is obtained by the winding number calculation. Right: Poisson's equation is solved with an immersed object represented using a 2D point cloud. (b) The in-out information is obtained by solving the Eikonal equation in addition to the solution to the Poisson's equation using the IBN framework.

Element framework to solve the Eikonal equation. The field solution to the Eikonal equation is a signed distance field. Once a signed distance field is obtained for the irregular boundary, we use a differentiable conditional function to create an accurate binary mask from the signed distance field.

Poisson's Equation with χ_w -based Geometry Loss:

The canonical Poisson's equation was introduced in Equation 2. In this section we apply IBN to solve the Poisson's equation with $f = 0$ and the boundary conditions defined as: $u = 1$, on Γ_o and $u = 0$, on Γ_B . This case mimics a steady heat transfer problem where Ω_o represents a heat source (of infinite capacity) and the outer boundary Γ_B represents a sink (of infinite capacity). The solution to Equation 2 along with the above f and the boundary conditions is the temperature field under those conditions. This case essentially refers to a large family of different problems where Γ_B can be any closed surface such that $\Omega_o \subset \Omega_B$. As discussed in Section 3, we consider the cases where such source object shapes are available as point cloud data, and our goal is to devise a fast neural method to use the point cloud data directly in analysis without having to go through a mesh generation process. Figure 7a shows the results of the winding number and the corresponding solution to the PDE.

Poisson's Equation with χ_e -based Geometry Loss:

In this case, along with the Poisson's Equation, we solve Eikonal equation $(1 + \tau)\|\nabla\phi\| - \tau(\nabla\phi) = 1$, $\tau \in [0, 0.5]$ with $\phi = 0$ at Γ_o . For this case, we simultaneously solve for both the PDEs and show the results in Figure 7b.